

THE KINETIC SUNYAEV-ZEL'DOVICH EFFECT FROM RADIATIVE TRANSFER SIMULATIONS OF PATCHY REIONIZATION

ILIAN T. ILIEV¹, UE-LI PEN¹, J. RICHARD BOND¹, GARRELT MELLEMA², PAUL R. SHAPIRO³
submitted to ApJ

ABSTRACT

We present the first calculation of the kinetic Sunyaev-Zel'dovich (kSZ) effect due to the inhomogeneous reionization of the universe based on detailed large-scale radiative transfer simulations of reionization. The resulting sky power spectra peak at $\ell = 2000 - 8000$ with maximum values of $[\ell(\ell + 1)C_\ell/(2\pi)]_{\max} \sim 1 \times 10^{-12}$. The peak scale is determined by the typical size of the ionized regions and roughly corresponds to the ionized bubble sizes observed in our simulations, $\sim 5 - 20$ Mpc. The kSZ anisotropy signal from reionization dominates the primary CMB signal above $\ell = 3000$. This predicted kSZ signal at arcminute scales is sufficiently strong to be detectable by upcoming experiments, like the Atacama Cosmology Telescope and South Pole Telescope which are expected to have $\sim 1'$ resolution and $\sim \mu\text{K}$ sensitivity. The extended and patchy nature of the reionization process results in a boost of the peak signal in power by approximately one order of magnitude compared to a uniform reionization scenario, while roughly tripling the signal compared with that based upon the assumption of gradual but spatially uniform reionization. At large scales the patchy kSZ signal depends largely on the ionizing source efficiencies and the large-scale velocity fields: sources that produce photons more efficiently yield correspondingly higher signals. The introduction of sub-grid gas clumping in the radiative transfer simulations produces significantly more power at small scales, and more non-Gaussian features, but has little effect at large scales. The patchy nature of the reionization process roughly doubles the *total* observed kSZ signal for $\ell \sim 3000 - 10^4$ compared to non-patchy scenarios with the same total electron-scattering optical depth.

Subject headings: radiative transfer—cosmology: theory—cosmic microwave background—intergalactic medium — large-scale structure of universe — radio lines

1. INTRODUCTION

The secondary anisotropies of the Cosmic Microwave Background (CMB) are emerging as one of the most powerful tools in cosmology. The small-scale anisotropies are probes of cosmological structures and are thus a valuable tool for studying their formation and properties. The key effect generating small-scale CMB anisotropies is the Sunyaev-Zel'dovich (SZ) effect (Zeldovich & Sunyaev 1969), produced by Compton scattering of the CMB photons on moving free electrons. When this is due to thermal motions the effect is referred to as thermal SZ effect (tSZ), while when it is due to the electrons moving with a net bulk peculiar velocity it is called kinetic SZ effect (kSZ) (Sunyaev & Zeldovich 1980). The former, coming largely from hot gas in low-redshift galaxy clusters, is the dominant effect, but has a different spectrum than the CMB primary anisotropies. The tSZ spectrum has a characteristic zero at ~ 217 MHz, so its contribution can in principle be separated. By contrast, kSZ anisotropies have a spectrum identical with that of the primary anisotropies. Separation of its effects is possible only by virtue of its different spatial structure. We consider the kSZ fluctuations as composed of two basic contributions, one coming from inhomogeneous reionization and the other

from the fully-ionized gas after reionization. The calculation of the patchy reionization contribution to the kSZ signal based on the first large-scale radiative transfer simulations of reionization is the main focus of this paper. This signal provides a signature of the character of reionization that will complement other approaches like observations of the redshifted 21-cm line of hydrogen and surveys of high- z Ly- α emitters (e.g. Scott & Rees 1990; Tozzi et al. 2000; Iliev et al. 2002, 2003; Ciardi & Madau 2003; Rhoads et al. 2003; Stanway & et al. 2004; Gnedin & Prada 2004; Furlanetto et al. 2004a; Mellema et al. 2006b; Malhotra & Rhoads 2006; Shapiro et al. 2006; Bunker et al. 2006; Furlanetto et al. 2006). In addition to better understanding of the physics of reionization, such studies could provide better constraints on the fundamental cosmological parameters, in particular on the primordial power spectrum of density fluctuations at smaller scales than are currently available.

The kSZ from a fully-ionized medium has been studied previously by both analytical and numerical means. When linear perturbation theory is used, the effect is associated with the quadratic nonlinearities in the electron density current and is usually referred to as the Ostriker-Vishniac effect (Ostriker & Vishniac 1986; Vishniac 1987). Calculating the full, nonlinear effect is much more difficult to do analytically, although some models have been proposed (e.g. Jaffe & Kamionkowski 1998; Hu 2000; Ma & Fry 2002; Zhang et al. 2004). This effect involves coupling of very large-scale to quite small-scale density fluctuation modes and thus requires a very large dynamic range in order to be simulated correctly.

¹ Canadian Institute for Theoretical Astrophysics, University of Toronto, 60 St. George Street, Toronto, ON M5S 3H8, Canada; iliev@cita.utoronto.ca

² Stockholm Observatory, AlbaNova University Center, Stockholm University, SE-106 91 Stockholm, Sweden

³ Department of Astronomy, University of Texas, Austin, TX 78712-1083, U.S.A.

$f_\gamma = 2000$ and 250 , respectively, and no sub-grid gas clumping, while f2000C and f250C adopt the same respective efficiencies, $f_\gamma = 2000$ and 250 , but also add a sub-grid gas clumping, $C(z) = \langle n^2 \rangle / \langle n \rangle^2$, which evolves with redshift according to

$$C_{\text{subgrid}}(z) = 27.466e^{-0.114z+0.001328z^2}. \quad (2)$$

The last fit was obtained from another high-resolution PMFAST N-body simulation, with box size $(3.5 \text{ h}^{-1} \text{ Mpc})^3$ and a computational mesh and number of particles of 3248^3 and 1624^3 , respectively. These parameters correspond to a particle mass of $10^3 M_\odot$ and minimum resolved halo mass of $10^5 M_\odot$. This box size was chosen so as to resolve the scales most relevant to the gas clumping - on scales smaller than these the gas fluctuations would be below the Jeans scale, while on larger scales the density fluctuations are already present in our computational density fields and should not be doubly-counted. The expression in equation (2) excludes the matter inside collapsed minihalos (halos which are too small to cool atomically, and thus have inefficient star formation) since these are shielded, unlike the generally optically-thin IGM. This self-shielding results in a lower contribution of the minihalos to the total number of recombinations than one would infer from a simple gas clumping argument (Shapiro et al. 2004; Iliev et al. 2005b,a). The effect of minihalos could be included as sub-grid physics as well, see Ciardi et al. (2006). This results in slower propagation of the ionization fronts and further delay of the final overlap. The halos that can cool atomically are assumed here to be ionizing sources and their recombinations are thus implicitly included in the photon production efficiency f_γ through the corresponding escape fraction.

3. KSZ FROM PATCHY REIONIZATION

The kSZ effect is the CMB temperature anisotropy along a line-of-sight (LOS) defined by a unit vector \mathbf{n} induced by Thomson scattering from flowing electrons:

$$\frac{\Delta T}{T_{\text{CMB}}} = \int d\eta e^{-\tau_{\text{es}}(\eta)} a n_e \sigma_T \mathbf{n} \cdot \mathbf{v}, \quad (3)$$

where $\eta = \int_0^t dt' / a(t')$ is the conformal time, a is the scale factor, $\sigma_T = 6.65 \times 10^{-25} \text{ cm}^{-2}$ is the Thomson scattering cross-section, and τ_{es} is the corresponding optical depth.

We calculate the kSZ anisotropy signal from our simulation data as follows. We first calculate the line-of-sight integral in equation (3) for each individual output time-slice of the radiative transfer simulation and for all LOS along each of the three box axes. The contribution to the total LOS integral from each light-crossing time of the box is then obtained by linear interpolation between the nearest results from the simulation output times. The individual light-crossing time contributions are then all added together to obtain the full LOS integral given in equation (3). All these integrals are done for each LOS through the box along the direction of light propagation, which allows us to produce kSZ maps, in addition to the statistical signals. In order to avoid artificial amplification of the fluctuations resulting from repeating the same structures along the line of sight, after each light-crossing time we randomly shift the box in the directions perpendicular to the LOS and rotate the box, so that the LOS

cycles the directions along the x, y and z axes of the simulation volume.

For comparison we also consider two simplified cases in addition to our simulations, the cases of instant and of uniform reionization. We define instant reionization as a sharp transition from completely neutral to fully-ionized IGM at redshift z_{instant} . We pick $z_{\text{instant}} = 13$, which yields the same integrated electron scattering optical depth as our simulation f250. We also define a ‘‘uniform reionization’’ scenario to be one that has the same time-dependent reionization history (and hence, also the same τ_{es}) as simulation f250, but spatially uniform (i.e. not patchy). We then derive the kSZ temperature fluctuations for these two scenarios using the same density and velocity data and same procedures as for the actual simulations. We consider these simplified models in order to demonstrate the effects of reionization being extended and patchy in nature.

4. RESULTS

4.1. kSZ maps

We show the kSZ maps of temperature fluctuations, $\delta T / T_{\text{CMB}}$, yielded by all of our cases in Figure 1. These have a total angular size of approximately $50' \times 50'$, corresponding to our computational box size. The resolution of the maps is that of the full radiative transfer grid (203×203 pixels), corresponding to pixel resolution of $\sim 0.25'$. All maps utilize the same color map in order to facilitate their direct comparison. The maps deriving from our simulations of inhomogeneous reionization (Figure 1, top and middle) all show fairly strong fluctuations, both positive and negative, of order $\delta T \sim 10 \mu\text{K}$ at angular scales of a few arcminutes ($\sim 10 \text{ h}^{-1} \text{ Mpc}$) and up to $\delta T \sim 20 \mu\text{K}$ at the full map resolution. The fluctuations are at somewhat smaller scales when the sources are less efficient photon producers (f250 and f250C), compared to the high-efficiency cases (f2000 and f2000C). The variations are noticeably enhanced when sub-grid gas clumping is included in the reionization model (f2000C and f250C) and there are a number of regions with very strong features. In comparison, the artificial models of instant and uniform reionization (Figure 1, bottom) show fluctuations with much lower amplitudes and with a less well-defined typical scale. Since these simple scenarios were constructed to produce the same total electron scattering optical depth as simulation f250 and they use the same density and velocity fields as the simulations, any observed differences are due to the patchiness of reionization. The lower signal in these last two cases is expected since the kSZ effect in uniformly-ionized gas exactly cancels in the first order of the linear theory (Kaiser 1984). This cancellation is broken when patchiness is present, however, which enhances the anisotropies.

The mean and rms of the temperature fluctuations for all cases are summarized in Table 1. Based on these, we see that, indeed, the uniform and instant reionization cases have means very close to zero, as expected, while the realistic, patchy reionization simulations yield mean temperature fluctuations that are low, of order $\sim 10^{-7}$, but not zero. The rms values are $\sim 10^{-6}$ for all patchy reionization cases and lower than that by factor of ~ 2 (~ 3) for the instant (uniform) reionization cases.

These observations based on the maps are confirmed by their corresponding pixel PDF distributions, shown

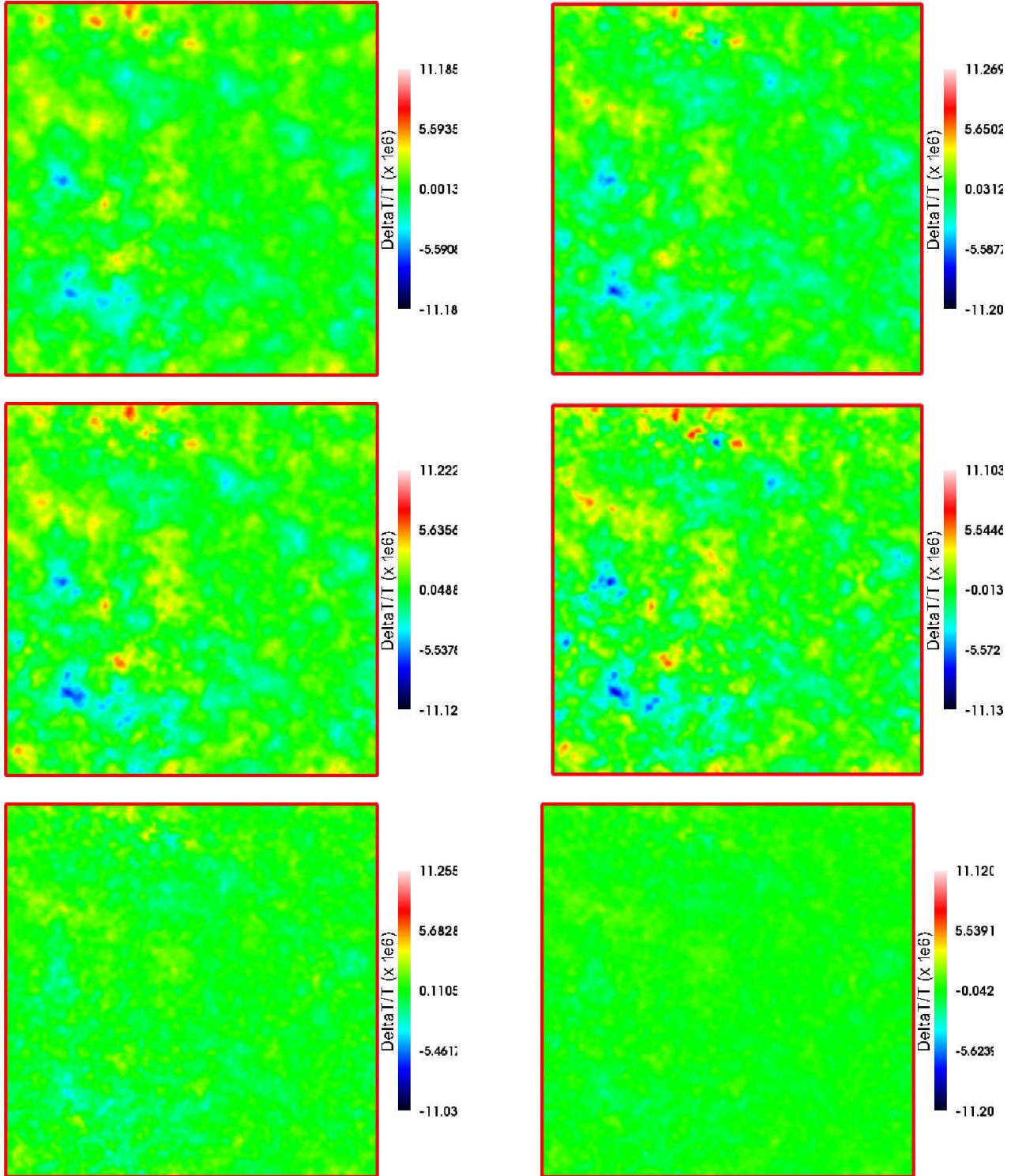


FIG. 1.— kSZ maps from simulations: f2000 (top left), f250 (top right), f2000C (middle left), f250C (middle right) instant reionization at $z_{\text{instant}} = 13$ which gives the same total electron scattering optical depth as simulation f250 (bottom left), and spatially-uniform reionization with the same reionization history and thus same total electron scattering optical depth as simulation f250 (bottom right). (Images produced using the Ifrit visualization package of N. Gnedin).

in Figures 2 and 3. On each panel we also plot the Gaussian distribution with the same mean and standard deviation. All distributions are surprisingly close to Gaussian around their mean values given the maps. However noticeable departures from Gaussianity do occur in the

wings of the PDFs. In particular, the PDFs for patchy reionization with sub-grid clumping (f2000C, and f250C) are significantly non-Gaussian. For the realization being considered here there is an over-abundance of bright regions by up to an order of magnitude compared to the

TABLE 1
MEAN AND RMS VALUES FOR $\delta T_{\text{kSZ}}/T_{\text{CMB}}$.

simulation	f2000	f2000C	f250	f250C	uniform	instant
mean	8.86×10^{-8}	9.88×10^{-8}	-2.17×10^{-7}	5.57×10^{-8}	-3.29×10^{-12}	-3.37×10^{-12}
rms	1.13×10^{-6}	1.22×10^{-6}	1.06×10^{-6}	1.09×10^{-6}	4.24×10^{-7}	6.67×10^{-7}

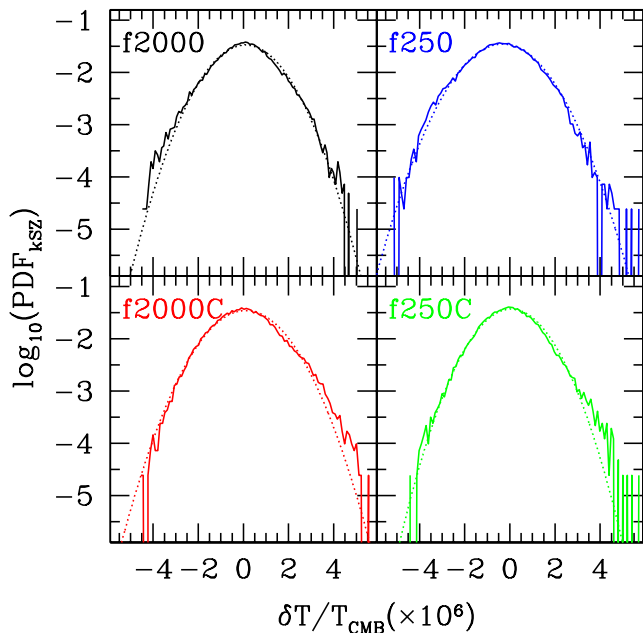


FIG. 2.— PDF distribution of $\delta T_{\text{kSZ}}/T_{\text{CMB}}$ (solid) vs. Gaussian distribution with the same mean and width (dotted) for our four simulations, as labelled.

corresponding Gaussian distributions. The reionization scenarios without sub-grid clumping show much weaker non-Gaussian features there. This indicates that the observed PDF of kSZ from patchy reionization may give us important information on the level of small-scale gas clumpiness during reionization. The PDFs derived from the uniform and instant reionization scenarios are significantly less wide than the simulated ones (which was also shown by their lower rms values, as was discussed above), and are also much closer to Gaussian.

4.2. Sky power spectra

In Figure 4 we show the 2D sky power spectra derived from our simulation data. These were obtained by calculating the sky power spectra for each box light-crossing time and adding these, which yields a smoother final result than would calculating the power spectrum directly from the final map. The kSZ anisotropy signal from inhomogeneous reionization dominates the primary CMB anisotropy above $\ell = 3000$. The sky power spectra peak strongly at $\ell = 3000 - 5000$, to a maximum of $[\ell(\ell+1)C_\ell/(2\pi)]_{\text{max}} \sim 7 \times 10^{-13}$ when the ionizing sources are highly-efficient (cases f2000 and f2000C).

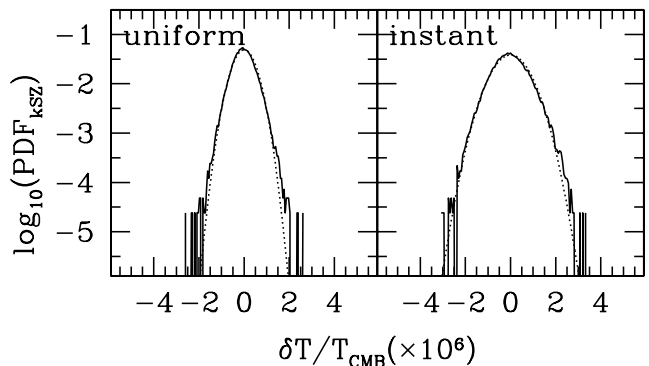


FIG. 3.— PDF distribution of $\delta T_{\text{kSZ}}/T_{\text{CMB}}$ (solid) vs. Gaussian distribution with the same mean and width (dotted) for the fiducial scenarios of uniform (left) and instant reionization (right).

The peak values for the simulations with lower-efficiency sources (f250 and f250C) are only slightly lower, at $[\ell(\ell+1)C_\ell/(2\pi)]_{\text{max}} \sim 4 \times 10^{-13}$, and the peaks are somewhat broader and moved to smaller scales, $\ell \sim 3000 - 7000$, than for the high-efficiency cases. The introduction of sub-grid gas clumping in the radiative transfer simulations produces significantly more power at small scales and slightly broader peaks when compared to the similar cases without sub-grid clumping. The scales at which the power spectra peak roughly correspond to the typical ionized bubble sizes observed in our simulations, namely $\sim 5 - 20$ Mpc comoving. These typical sizes depend on the assumed source efficiencies and sub-grid clumping. At large scales the patchy kSZ signal depends only on the source efficiencies, being higher for more efficient photon emitters, since these tend to produce larger ionized regions on average.

In contrast, the uniform reionization scenario (with the mean reionization history of simulation f250) yields a kSZ signature which is much lower than the non-uniform reionization scenarios, indicating a very large boost of the signal due to the effects of patchiness. The boost is largest, approximately one order of magnitude, at and above the typical scale of the patches ($\ell < 7000$), but it still exists at smaller scales, where it is a factor of two or more. The other simplified scenario, of instant reionization with the same integrated optical depth as f250, produces larger kSZ anisotropy than a uniform reionization does. However, it is still well below the realistic patchy reionization signals, by factor of ~ 3 for $\ell < 7000$. At smaller scales the reionization signal from the instant reionization scenario becomes similar to the ones from

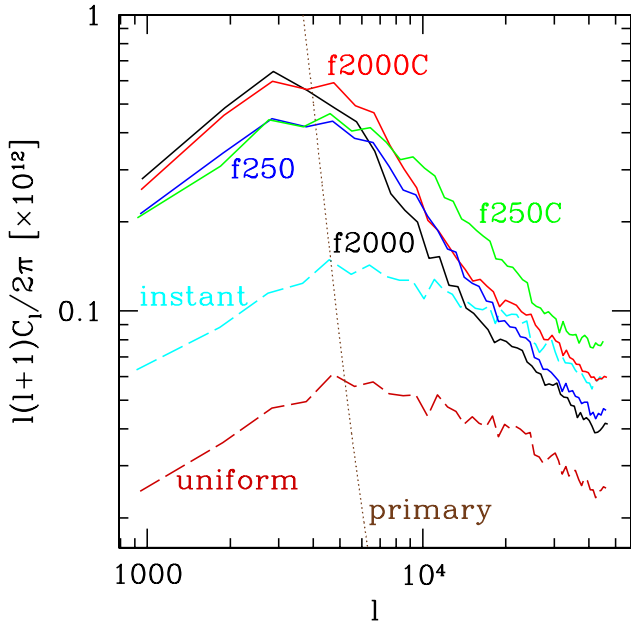


FIG. 4.— Sky power spectra of $\delta T_{\text{kSZ}}/T_{\text{CMB}}$ fluctuations resulting from our simulations: f2000 (black), f250 (blue), f2000C (red) and f250C (green). For comparison, we also show the results from simple models which utilize the same density and velocity fields as the actual simulations, but different assumptions about the gas ionization in space and time, a uniform reionization with the same reionization history as simulation f250 (dashed, dark red) and an instant reionization model with the same integrated optical depth τ_{es} as simulation f250 (dashed, cyan). The primary CMB anisotropy signal is also shown (dotted, brown).

simulated non-uniform reionization. The distribution of the power in these two simplified scenarios is much flatter, with less indication of a characteristic scale. This implies that the sharp peaks yielded by the inhomogeneous reionization scenarios are dictated by the size of the ionized patches, since both the density and the velocity fields are shared among our models. This point is discussed further in § 4.3.

This behavior can be understood further by considering the contributions from different redshift intervals to the integrated signal. In Figure 5 we show the contributions to the total signal from different redshift intervals for simulation f250, as well as the uniform and instant reionization scenarios. We plot the contribution from every three light-crossing times of the box, corresponding roughly to $z > 15$, $15 > z > 11$ and $z < 11$. The mass-weighted ionized fraction in the highest redshift interval is $x_m < 0.01$, and consequently its contribution to the kSZ effect (case f250, bottom curve) is low, with a maximum of $\sim 10^{-14}$. This high-redshift contribution is strongly peaked at very small scales ($\ell > 10^4$), reflecting the fact that at that time the typical ionized bubble is still fairly small, less than a few Mpc in size. The contribution from the middle redshift interval, $11 < z < 15$, (corresponding to $0.8 > x_m > 0.01$) peaks at roughly the same scales as the total signal. This interval contributes about half of the total signal around the peak, but a smaller fraction at scales above and below that. A half or more of the integrated kSZ signal at all scales is con-

tributed by the lowest redshifts ($z < 11$, $x_m \gtrsim 0.8$). The low-redshift power spectrum is fairly flat, with a weak peak at relatively large scales, $\ell \sim 2000$. This late-time contribution resembles the results for the two homogeneous scenarios, but has higher amplitude and a different shape. This indicates that even at late times, when most of the IGM is already ionized, the patchiness still plays an important role in assembling the kSZ signal.

In the homogeneous (uniform and instant) reionization cases the shape of the power spectra is essentially the same for all redshift intervals, quite flat, with a broad peak at $\ell \sim 5000$. The signal from the uniform reionization scenario is completely dominated by the lowest redshifts, with less than a few per cent coming from the middle redshift interval, and essentially no contribution from high redshifts. Since the velocity and density fields are shared, the instant reionization scenario contributions differ from the corresponding ones from the uniform scenario only by being weighted by the ionized fraction in the uniform case. The instant reionization scenario assumes full ionization after $z_{\text{instant}} = 13$ and fully-neutral gas before that. Thus, as a consequence to the kSZ signal being stronger at later times, the instant reionization integrated signal is higher as well. For comparison, we also show the corresponding redshift-binned results from the model of Zhang et al. (2004) (see § 4.3) against our results from the instant reionization scenario. The two results agree well at small scales, in the potentially-observable range.

4.3. Linear theory and large-scale velocity field corrections

In linear theory the velocity and density perturbations at redshift z are related through the continuity equation:

$$\tilde{v}(\mathbf{k}, t) = \frac{ia(t)}{k^2} \frac{\dot{D}(t)}{D(t)} \mathbf{k} \tilde{\delta}(\mathbf{k}, t), \quad (4)$$

where $a = (1+z)^{-1}$ is the scale factor, and $D(t)$ is the growth factor of linear perturbations, which for a flat Λ CDM background cosmology is given by

$$D(z) = \frac{5\Omega_0 E(z)}{2} \int_z^\infty \frac{1+z'}{[E(z')]^3} dz', \quad (5)$$

with $E(z) = H(z)/H_0 = [\Omega_0(1+z)^3 + \Omega_\Lambda]^{1/2}$, where $H(z)$ and H_0 are the values of the Hubble constant at redshift z and at present, respectively. In terms of the power spectra of the density, $P_{\delta\delta}$, and the velocity, P_{vv} , equation (4) can be re-written as

$$P_{vv}(k, t) = \frac{a^2(t)}{k^2} \left[\frac{\dot{D}(t)}{D(t)} \right]^2 P_{\delta\delta}(k, t), \quad (6)$$

or

$$\Delta_v^2(k, t) = \frac{a^2(t)}{k^2} \left[\frac{\dot{D}(t)}{D(t)} \right]^2 \Delta_\delta^2(k, t), \quad (7)$$

where we defined

$$\Delta_\delta^2 \equiv \frac{k^3}{2\pi^2} P_{\delta\delta} \quad (8)$$

and

$$\Delta_v^2 \equiv \frac{k^3}{2\pi^2} P_{vv}, \quad (9)$$

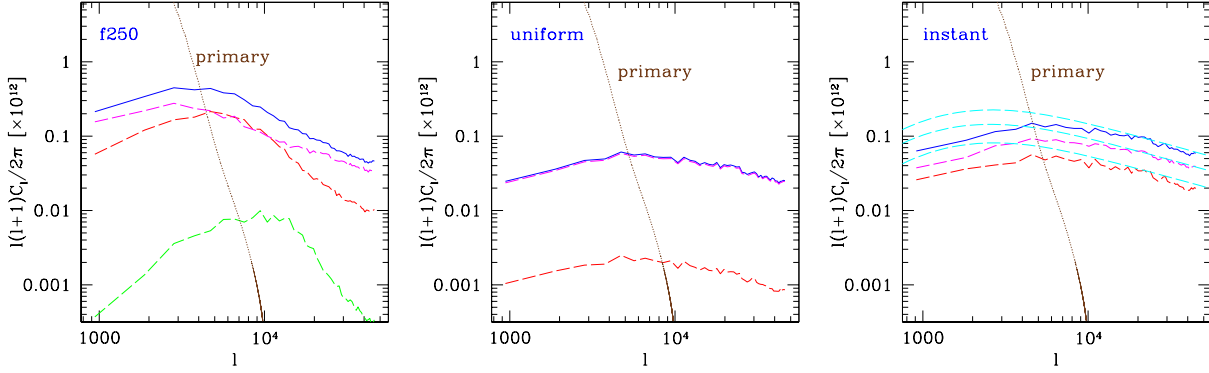


FIG. 5.— Contributions to the total kSZ signal (blue) from different redshifts for case f250 (left), uniform (middle) and instant reionization (right). Shown are the signals for every three box light crossing times, roughly corresponding to (bottom to top on the left) redshifts $z > 15$ (green), $15 > z > 11$ (red), $z < 11$ (magenta). In the last two cases the $z > 15$ contribution is very low (uniform) or zero (instant) and thus not show. For comparison, on the last panel we also show the corresponding redshift-binned results from the model of Zhang et al. (2004) (see § 4.3).

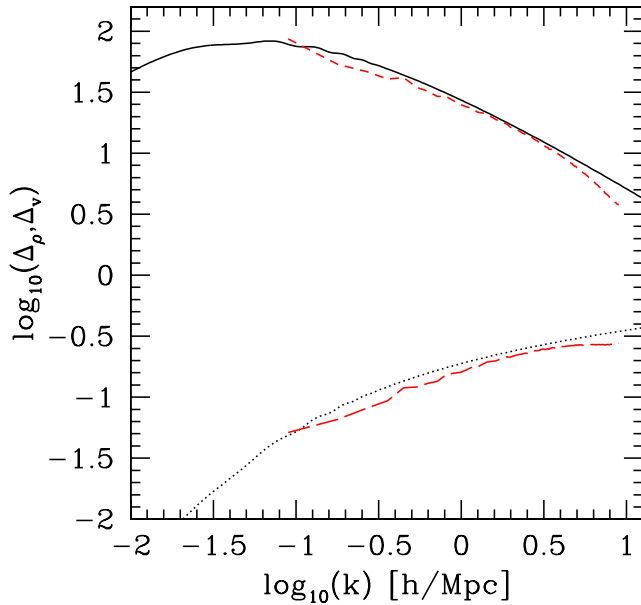


FIG. 6.— Linear-theory power spectra at redshift $z = 13.6$ of the density field (dotted, black) and velocity field (in km s^{-1} ; solid, black) compared to the simulation results for the density (long-dashed, red) and velocity (short-dashed, red).

which would be our notation for the power spectra hereafter. The quantities Δ_δ^2 and Δ_v^2 are the power per logarithmic interval of the wave-number k of the density and velocity fields, respectively.

Using equation (5) it is straightforward to show that

$$\begin{aligned} \frac{\dot{D}}{D} &= \frac{\ddot{a}}{\dot{a}} - \frac{\dot{a}}{a} + \frac{5\Omega_0 \dot{a}}{2a} \frac{(1+z)^2}{[E(z)]^2 D(z)} \\ &= -\frac{3H_0\Omega_0(1+z)^3}{E(z)} \left[1 - \frac{5}{3(1+z)D(z)} \right]. \end{aligned} \quad (10)$$

Substituting equation (10) into equation (7) we finally find

$$\Delta_v^2(k, z) =$$

$$\frac{\Delta_\delta^2(k, z)}{k^2} \frac{9H_0^2\Omega_0^2(1+z)^4}{4E^2(z)} \left[1 - \frac{5}{3(1+z)D(z)} \right]^2. \quad (11)$$

In Figure 6 we show the CMBfast density power spectrum at redshift $z = 13.6$, and the corresponding linear-theory velocity power spectrum given by equation (11), along with the density and velocity power spectra obtained from our N-body simulation data (re-gridded to our radiative transfer grid of 203^3). Comparison of the two sets of data shows a good agreement between them and indicates that at these scales and redshifts our density and velocity fields are clearly still in the linear regime. Note, however, that the bulk velocities derived from the simulation data do include the non-linear effects at smaller scales, up to the full resolution of the underlying N-body simulation, at 3248^3 cells, or $\sim 30 h^{-1}$ kpc comoving per cell, averaged at the radiative transfer grid resolution. The velocity power spectra were derived from the simulated data by first calculating the power spectrum of each of the three velocity components and then averaging these, which minimizes the variance at large scales.

The velocity power spectrum has a broad peak at fairly large scales, $k \sim 0.01 - 0.1 h \text{Mpc}^{-1}$, corresponding to scales $\sim 60 - 600 \text{Mpc } h^{-1}$. Thus, our simulation volume is sufficiently large to reach this velocity peak, but is still missing some velocity power from the largest scales. We estimate the missing power as follows. The rms of the velocity field is given by

$$v_{\text{rms}}^2 = \int \Delta_v^2(k) d \ln(k). \quad (12)$$

Thus, integrating over the full linear power spectrum yields the total power in the velocity field, $v_{\text{rms,tot}}^2$ in the linear theory. A finite simulation box of size L_{box} would not include the modes with wave-numbers below $k_{\text{min}} = 2\pi/L_{\text{box}}$. Integrating Δ_v^2 over the wave-numbers $k > k_{\text{min}}$, we obtain the total velocity power for a given box size. The results are shown in Figure 7, where we plot the fraction of total linear-theory velocity power $v_{\text{rms,box}}^2/v_{\text{rms,tot}}^2$ present in a simulation box vs. the box size L_{box} . A simulation of volume $(100 h^{-1} \text{Mpc})^3$ would thus be missing about $\sim 50\%$ of the total v_{rms}^2 velocity

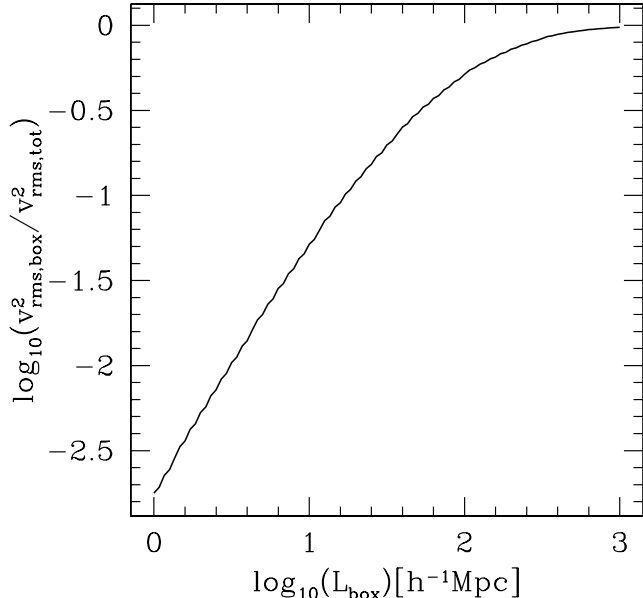


FIG. 7.— Fraction of total linear-theory velocity power $v_{\text{rms,box}}^2/v_{\text{rms,tot}}^2$ present in a simulation box of size L_{box} vs. L_{box} .

power as given by the linear theory. Simulations with smaller volumes would miss much larger fraction of the velocity power, $\sim 70\%$ for $50 h^{-1}\text{Mpc}$ box, $\sim 90\%$ for $20 h^{-1}\text{Mpc}$ box, and over 99% for $4 h^{-1}\text{Mpc}$ box.

The large-scale bulk motions not included in our simulation occur on scales of ~ 100 Mpc or larger, well above the characteristic size of the ionized patches (~ 10 Mpc or less) (Iliev et al. 2006b, see also Figure 9), thus on such scales the reionization patchiness averages out and the ionization fraction approaches the mean for the universe. We can approximately account for the missing large-scale velocity power as follows. At each light-crossing time we can assume that the whole simulation volume is moving with some random velocity, \bar{v}_{box} . In order to account for the missing velocity power, the value of the component of this random velocity at redshift z along the line-of-sight is given by

$$\bar{v}_{\text{box}}(z) = v_{\text{rms,missing}}(-2 \ln q)^{1/2} \cos(2\pi\theta), \quad (13)$$

where $v_{\text{rms,missing}} \equiv [v_{\text{rms,tot}}(z)^2 - v_{\text{rms,box}}(z)]^{1/2}$, and q and θ are uniformly-distributed random variables between 0 and 1. The form of equation (13) ensures that $\bar{v}_{\text{box}}(z)$ is a Gaussian-distributed random variable with a zero mean and rms of $v_{\text{rms,missing}}$ (Box & Muller 1958). In terms of the contribution from this redshift to the temperature anisotropy this yields

$$\left(\frac{\Delta T}{T_{\text{CMB}}}\right)_{\text{tot}}(z) = \left(\frac{\Delta T}{T_{\text{CMB}}}\right)_{\text{box}}(z) + \tau_{\text{es}}(z) \frac{\bar{v}_{\text{box}}(z)}{c}, \quad (14)$$

where $\tau_{\text{es}}(z)$ is the corresponding contribution to the total electron-scattering optical depth. Note that for uniform reionization the effects from large-scale velocity fields would exactly cancel, since the flow is potential (Kaiser 1984). However, the patchiness breaks this cancellation and the large-scale velocities increase the signal

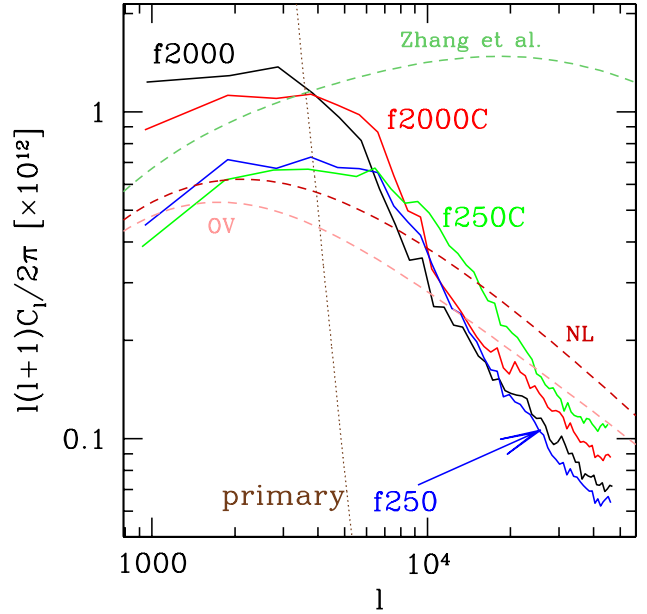


FIG. 8.— Sky power spectra of $\delta T_{\text{kSZ}}/T_{\text{CMB}}$ fluctuations from the epoch of reionization based on our simulations, f2000 (black), f250 (blue), f2000C (red) and f250C (green), corrected for the missing velocity field power compared to the after-reionization kSZ signals (assuming overlap at $z_{\text{ov}} = 8$): linear Ostriker-Vishniac effect, labelled 'OV' (long-dashed, pink), the same, but using the nonlinear power spectrum of density fluctuations, labelled 'NL' (long-dashed, dark red) and a fully-nonlinear model matched to high-resolution hydrodynamic simulations of Zhang et al. (2004), labelled 'Zhang et al' (short-dashed, dark green). The primary CMB anisotropy signal is also shown (brown, dotted).

by increasing the ionized bubble velocities along the LOS. The ionized regions are at much smaller scale than these large-scale velocities and uncorrelated with them, thus avoiding the usual cancellation.

The power spectra with large-scale velocity corrections included are shown in Figure 8. For comparison, we also show three representative calculations of the post-reionization contribution from fully-ionized gas after reionization: the quadratic-order Ostriker-Vishniac effect (Vishniac 1987) expressed in terms of a product of the linear power spectra; the same expression, but with the nonlinear density power spectrum substituted for one of the linear ones, which partially accounts for the nonlinear effects; and the recent detailed nonlinear model of Zhang et al. (2004). The last three models are rescaled to our adopted cosmology using $\ell(\ell+1)C_\ell \propto \sigma_8^5$ (Zhang et al. 2004), and assume reionization overlap at $z_{\text{ov}} = 8$, to allow for direct comparison. Confronting first the three post-reionization models, we see that they agree fairly well at large, linear scales, but strongly diverge, by up to one order of magnitude at small scales, where the nonlinearities become very important. Including the corrections due to the nonlinear density power spectrum yields modestly higher kSZ signal than the linear OV calculation, and similar power spectrum shape overall. Both peak at roughly the same scale, $\ell \sim 2000$. In contrast, the Zhang et al. (2004) result finds much larger signal, especially at small scales, which peaks at $\ell \sim 20,000$. Compared to our patchy reionization kSZ predictions, all

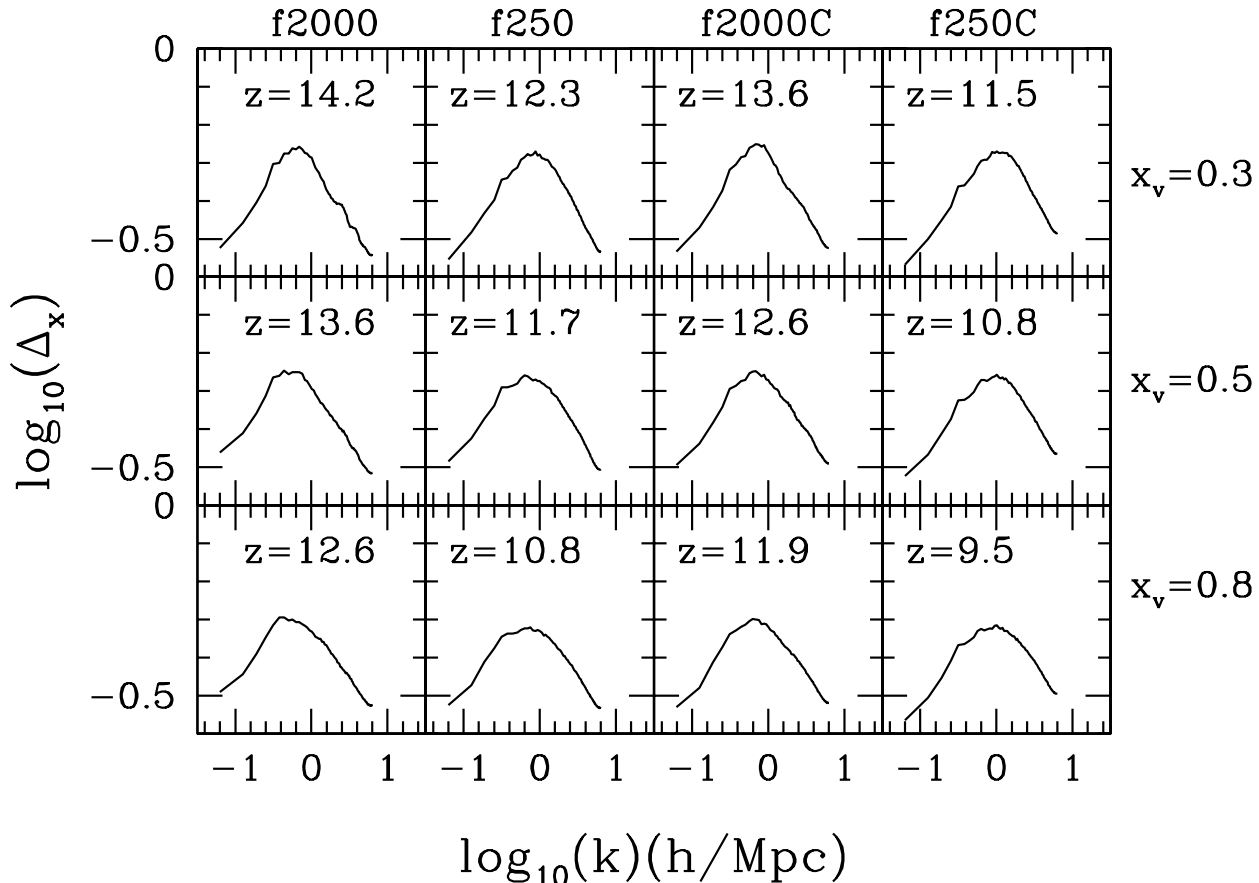


FIG. 9.— Power spectra, Δ_x of the ionized/neutral fraction at volume ionized fractions $x_v = 0.3$ (top), $x_v = 0.5$ (middle), and $x_v = 0.8$ (bottom) for all of our simulations, as indicated on top of each column. The corresponding redshifts are indicated on each panel.

uniform-ionization power spectra are much less sharply peaked, i.e. they lack a well-established characteristic scale. In terms of their peak values, the OV and OV with nonlinear corrections models yield values lower than any of our patchy reionization results, while Zhang et al. (2004) find a similar signal around the patchy power spectra peaks. At small scales ($\ell > 10^4$) the patchy reionization kSZ signals are similar to or lower than the OV result and are much lower than the expected full nonlinear post-reionization contribution. Thus, the best range to aim for when attempting to detect the patchy reionization signal is $\ell = 3000 - 10^4$.

4.4. Characteristic scales and LOS spectra

The characteristic scale corresponding to the peak of the power spectra in Figure 8 is largely dictated by the typical scales of the ionized bubbles, since, as we discussed in § 4.3, the velocity and density are in the linear regime and do not have characteristic scales within the range corresponding to our simulation volume. However, the ionized patches do have a typical scale. In Figure 9 we show Δ_x , the power spectrum of the ionized fraction (which is the same as the one of the neutral fraction) for all of our simulation cases at the redshifts when the volume ionized fractions are $x_v = 0.3, 0.5$ and 0.8 . In

all cases the power spectra peak around wave-numbers $k \sim 1 \text{ hMpc}^{-1}$, which scale corresponds to $\ell \sim 7000$. As reionization progresses, the peak moves gradually to slightly larger scales, resulting in a moderate widening of the peak of the kSZ temperature anisotropy sky power spectra and slightly less well-defined typical scale than seen in the single-redshift 3D power spectra. In order to quantify the power spectra evolution better, in Figure 10 we show the evolution vs. redshift of the peak amplitude, $\Delta_{x,max}$, the scale at which it occurs, k_{max} , and the effective width of the peak, given by

$$\text{width} = \bar{k} \sinh \left\{ \left[\overline{\delta(\ln k)^2} \right]^{1/2} \right\} \quad (15)$$

where

$$\overline{\delta(\ln k)^2} = \frac{1}{x_{\text{rms}}^2} \int [(\ln k)^2 - (\overline{\ln k})^2] \Delta_x^2 d \ln k. \quad (16)$$

Here

$$\bar{k} = \exp(\overline{\ln k}) = \exp \left[\frac{1}{x_{\text{rms}}^2} \int (\ln k) \Delta_x^2 d \ln k \right] \quad (17)$$

and

$$x_{\text{rms}}^2 = \int \Delta_x^2 d \ln(k), \quad (18)$$

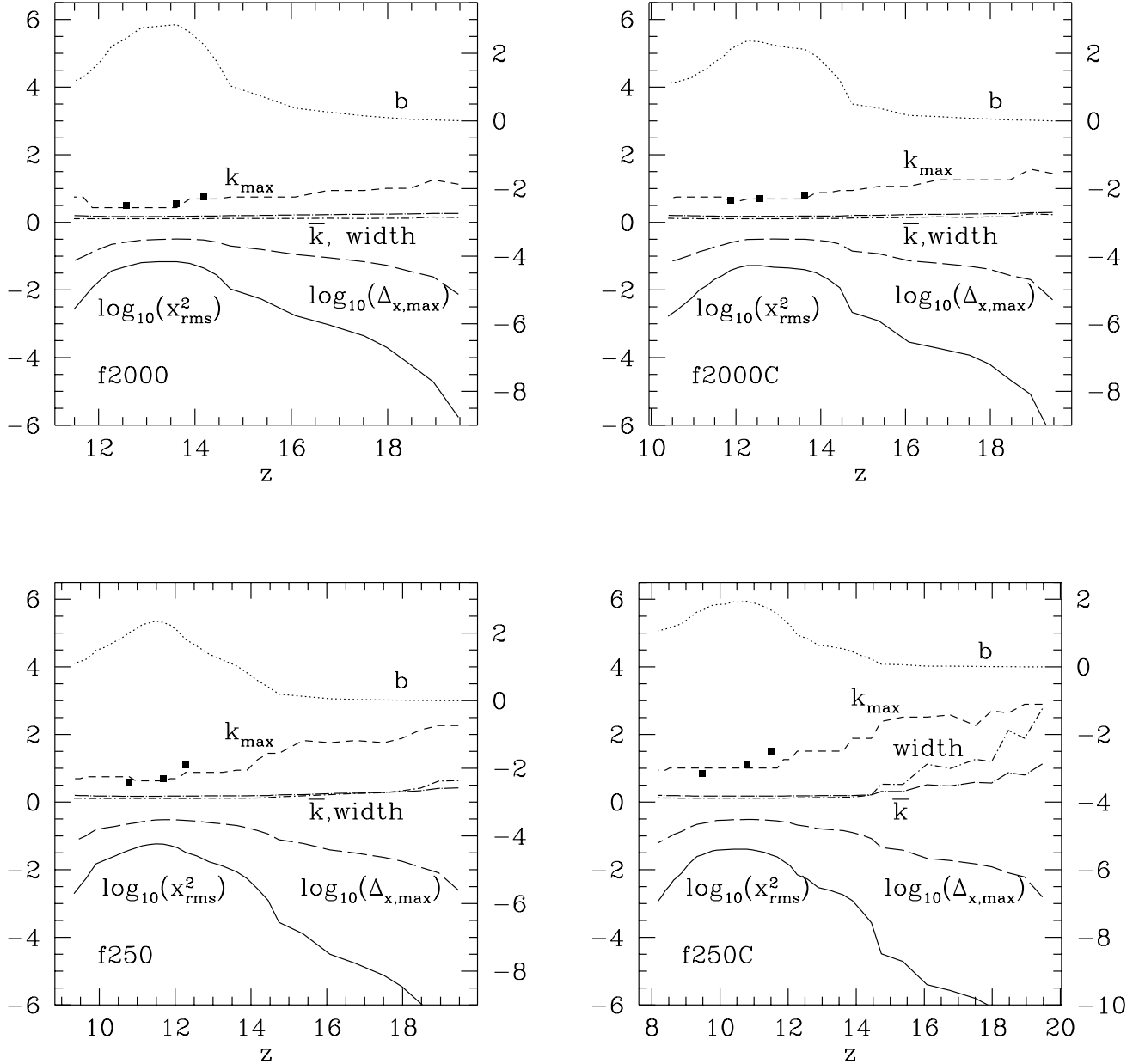


FIG. 10.— Evolution of Δ_x . Plotted are the peak value, $\Delta_{x,max}$, and the scale at which it occurs, k_{max} , its effective width, and the corresponding rms, x_{rms} for all simulations, as labelled. We also show the bias, $b(z)$, at large scales of the ionized density with respect to the underlying density field (values indicated on the right axis) and \bar{k} (see text for details). The values of $k_0/2$, where k_0 is the value of the characteristic ionized bubble scale which give a good fit to the $W(k)$ window function at large scales are also indicated for each case (black squares; see text for details).

which gives the total integrated power per logarithmic interval. We also show \bar{k} (in $h^{-1}\text{Mpc}$) and x_{rms}^2 . The amplitude of the peak initially rises, peaking at the point of maximum patchiness, $x_m \approx 0.5$, and slightly decreases thereafter. The scale of the peak, k_{max} , (in $h^{-1}\text{Mpc}$) steadily increases in time, as the typical ionized regions grow. Approximate linear fits (in the form $a + bz$) to $k_{max}(z)$ are given by $a = -0.528$ (-0.329, -1.135, -0.847) and $b = 0.085$ (0.089, 0.17, 0.19) for simulation f2000 (f2000C, f250, f250C). The effective width of

the power spectra and \bar{k} are largely constant and roughly equal to each other, except for simulation f250C at early times. Finally, the rms initially strongly rises, peaking at slightly later times than the patchiness itself peaks (at $x_m \approx 0.6$).

During the later stages of reionization ($x_m > 0.3$), which contribute most of the kSZ signal the ionized density fluctuations at large scales are proportional to the density fluctuations with a bias coefficient $b(z)$ (Iliev et al. 2006b, see also Figure 11. Note however that

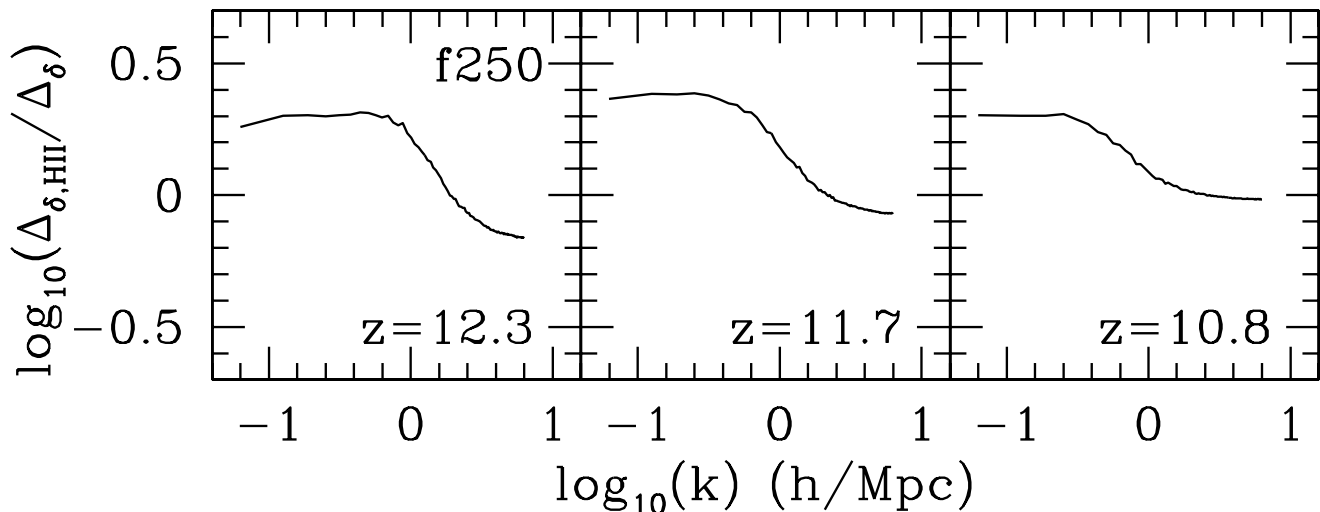


FIG. 11.— Ratio of the power spectra of the ionized density and the total density, $\Delta_{\delta,HII}/\Delta_{\delta}$ for simulation f250 at volume ionized fractions $x_v = 0.3$ (left), $x_v = 0.5$ (middle), and $x_v = 0.8$ (right). The corresponding redshifts are indicated on each panel.

this is not the case at earlier times, when the ionized regions are relatively small and isolated and do not follow the large-scale density perturbations.). Based on this fact we can derive a handy approximate expression for the power spectrum of the ionized gas density, $\Delta_{\delta,HII}$, as follows. Let

$$\Delta_{\delta,HII}(k, z) = b(z)W(k, z)\Delta_{\delta}(k, z), \quad (19)$$

where $W(k, z)$ is some window function asymptoting to 1 at large scales. We recognize that because of the zero or one nature of reionization (i.e. a region is either ionized or neutral when ionization fronts are unresolved, as is the case here), the random field $\delta n_e/\bar{n}_e$ is more complex than this relation between the power spectra indicates. However, it is reasonable to expect that for low k , the electron density structure will have such a proportionality, with the window function being related to a quadratic superposition of form factors for the various H II patches. If the reionization contribution from dense regions is lessened because of negative feedback from earlier ionizers on nearby galaxies, a situation we have ignored, the relation could be considerably modified. In spite of such complications, a simple relationship characterized by a characteristic scale related to the average size of the H II regions turns out to prevail as we now show.

The bias $b(z)$ is readily calculated from the simulation data (at the largest scale available from our simulation volume) and is shown in Figure 10 (values shown on the right axis). The bias starts close to zero since very little of the gas is ionized, and has a peak value of 2-3, reached again around the time of maximum patchiness. For redshifts around the time of maximum patchiness (for mass-weighted ionized fraction $0.3 < x_m < 0.8$) and at large scales ($k \gtrsim 1 - 2$) the window function $W(k, z)$ is reasonably well-fit (within factor of ~ 2 , and generally much better) by the following functional form:

$$W(k, z) = \frac{1}{1 + k^2/k_0^2(z)} \quad (20)$$

where $k_0(z)$ is a characteristic scale parameter which gives the best fit at the turnover. Samples of this window

function, $b(z)W(k, z)$, for simulation f250 are shown in Figure 11. At small scales this function turns over and the above fit is not applicable. The values of $k_0(z)/2$ at $x_m = 0.3, 0.5$ and 0.8 (in $h^{-1}\text{Mpc}$) are shown in Figure 10 (squares). They are very close to the scale at which the ionized fraction power spectra peak, k_{max} .

The addition of the missing large-scale velocity power outlined in the previous section boosts the sky power spectra at all scales, but especially at the largest ones, which further widens the peak. Nonetheless, the characteristic ionized bubble scale remains imprinted on the final results through their peak at $\ell \sim 2000 - 9000$.

To gain some further insight in the complex nature of the derived kSZ signal, in Figures 12 and 13 we show some sample line-of-sight (LOS) cuts through the simulation volume (simulation f250) of the density field in units of the mean, n_H/\bar{n}_H , ionized fraction, x_H , electron number density in units of the mean gas density, $n_e/\bar{n}_H = x_H n_H/\bar{n}_H$, velocity component along that LOS, v_x , and the accumulation of the kSZ temperature anisotropy integral (from left to right), $\Delta T_{\text{kSZ}}(< x)$. Early in the evolution ($z = 13.62$; Figure 12) the H II regions tend to be associated with high-density peaks, where the first halos (ionizing sources) form (inside-out reionization scenario). The ionized fraction distribution acts as a filter, picking the density field portions that would contribute to the CMB temperature anisotropies. The ionized regions are correlated with the high-density peaks (inside-out reionization), but the correlation is not perfect, there are density peaks which still remain neutral, while at the same time there are ionized regions which have a low overdensity, or are even underdense. The velocity field fluctuations are dominated by the largest scales and are generally not closely correlated with the density field or the ionized fraction. The velocity field determines the sign of the contribution of a given ionized region to the total temperature anisotropy. A number of different situations can be observed in our data. For example, in Figure 12 (left) the ionized regions are relatively closely spaced together, separated by

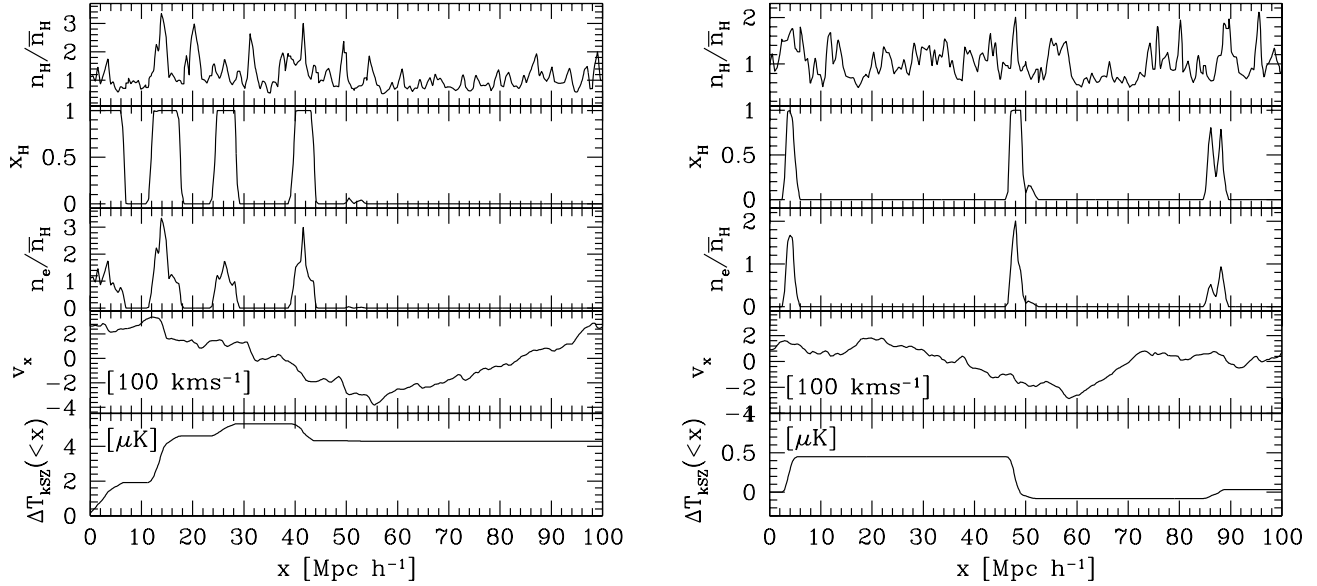


FIG. 12.— LOS cuts through the simulation volume (simulation f250) at $z = 13.622$ at which time the volume-weighted ionized fraction is $x_v = 0.095$, and the mass-weighted one is $x_m = 0.12$.

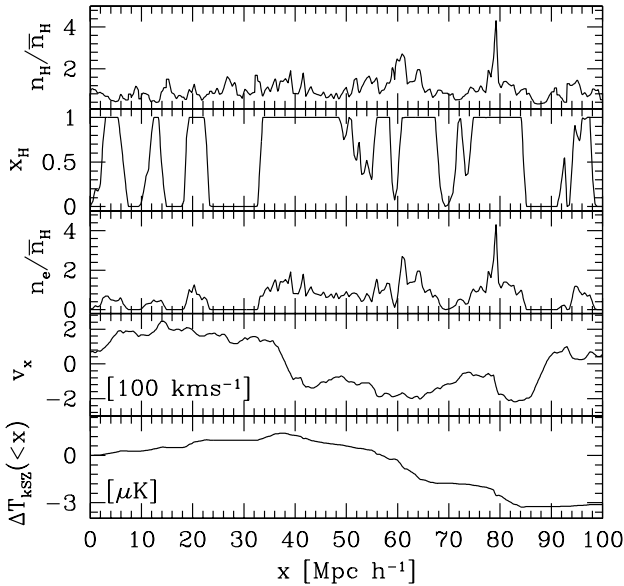


FIG. 13.— LOS cuts through the simulation volume (simulation f250) at $z = 11.310$ ($x_v = 0.66$, $x_m = 0.70$).

~ 10 Mpc, falling within the same large-scale velocity fluctuation. All H II regions except one are moving in the positive direction, resulting in a relatively large integrated temperature anisotropy of $\sim 4.4 \mu\text{K}$. The other sample case from the same redshift (Figure 12, right) includes three ionized regions along the LOS. These are separated by 40-50 moving Mpc, and thus correspond to completely uncorrelated density fluctuations. The ve-

locity field does not appear to correlate them, either, but nonetheless the temperature anisotropies they produce happen to almost exactly cancel each other, resulting in $\Delta T_{\text{kSZ}} \approx 0$ along that LOS. At later times (Figure 13) most of the volume is already ionized and each LOS encounters a number of ionized regions, but ultimately almost all of the total signal is contributed by the two highest-density peaks along the LOS, both of which here happen to move in the negative direction, while the contributions of the multiple other H II regions largely cancel each other. Once again, the density and velocity fields are not correlated. The ionized fraction is less correlated with the high-density regions than at early times. These examples demonstrate some of the complexities one has to deal with when trying to derive the kSZ signal from patchy reionization analytically, underscoring the need for large-scale simulations of this effect.

5. COMPARISONS TO PREVIOUS WORK

Previous simulations of the kSZ effect from patchy reionization (Gnedin & Jaffe 2001; Salvaterra et al. 2005) predicted significantly lower kSZ signals than the ones we find. Their power spectra reach maximum values of $[\ell(\ell+1)C_\ell/(2\pi)]_{\text{max}} \sim 2 \times 10^{-14}$ and $\sim 1.6 \times 10^{-13}$, respectively, compared to $[\ell(\ell+1)C_\ell/(2\pi)]_{\text{max}} \sim 1 \times 10^{-12}$ for our simulations. This discrepancy is due to the small volumes used in these simulations. As we showed in § 4.3 considering small volumes significantly reduces the power in the velocity field fluctuations. At the scale of the simulation box the bulk velocities are zero by definition, and the density is the mean one for the universe, thus any larger-scale fluctuations are not included, and the ones close to the box size are underestimated. The reionization patchiness imprints its characteristic scale on the density and velocity fluctuations, effectively smoothing the small-scale fluctuations below the typical

bubble sizes. On the other hand, the large-scale fluctuations still should contribute to the kSZ signal, since the H II regions are moving with the large scale bulk motions.

In addition to the missing large-scale power, these earlier reionization simulations also did not follow sufficient volumes to properly sample the size distribution of the ionized bubbles. The typical sizes of these ionized patches are of order 5-20 comoving Mpc, and become even larger at later times. These large characteristic bubble scales are result of the strong clustering of ionizing sources at high redshifts. Capturing the full bubble size distribution requires simulation volumes of order $(100 h^{-1} \text{Mpc})^3$ (Iliev et al. 2006b), and as a result the kSZ power spectra found by the smaller-box reionization simulations were largely flat, with no clear characteristic scale.

Several semi-analytical models for calculating the kSZ signature of patchy reionization have been proposed in recent years (Gruzinov & Hu 1998; Santos et al. 2003; McQuinn et al. 2005). Gruzinov & Hu (1998) proposed a very simple model, whereby the ionized patches are randomly distributed and have a given characteristic size R . Furthermore, they assumed that the density, velocity and ionization fraction fields are all uncorrelated with each other. The ionized fraction auto-correlation function is approximated as a Gaussian with rms given by the (fixed) characteristic H II region size. Under these assumptions the kSZ power spectrum can be calculated analytically. The quantitative details of the signal predicted by this model depend on the assumptions made about the typical ionized patch size, and the time and duration of reionization, but generically it predicts a distribution which is very strongly peaked, more so than our simulations find. This is related to the assumed Gaussian distribution around a fixed characteristic size of the ionized patches. The actual simulations also find a characteristic size for the ionized bubbles, but one that is also evolving with redshift, and different size distributions around it, which yields somewhat less sharp peaks than this analytical model predicts.

Santos et al. (2003) proposed another simple model for the reionization patchiness, which assumes that the correlation function of the ionized patches is proportional to the one for the density field, with a bias factor which is time-dependent, but not scale-dependent. The power is filtered at small scales, below the typical size of the ionized bubbles using a Gaussian filter in k-space. The time-dependence of the typical size of the ionized patches is assumed to be proportional to $[1 - x_m(t)]^{-1/3}$, where $x_m(t)$ is the mean mass-weighted ionized fraction at time t . The last function is based on the semi-analytical models of reionization of Haiman & Holder (2003). The resulting kSZ power spectra are fairly flat, with much less well-defined characteristic scale than our simulation results, as should be expected based on the quickly-evolving typical patch size assumed in this model. The peak amplitudes of the results is somewhat higher than the ones we find, by factors of $\sim 2 - 3$, probably due to their assumed values of the effective bias.

More recently, McQuinn et al. (2005) applied the semi-analytical reionization model of Furlanetto et al. (2004b) to estimate the kSZ signal. They found lower fluctua-

tions in their “single reionization episode” models (by factor of ~ 3), although these models have similar mean reionization histories (i.e. evolution of the mean volume-weighted ionized fraction) to our simulations. Their results also predict a peak at somewhat larger scales ($\ell \sim 2000$) than ours ($\ell \sim 2000-9000$). Their “extended reionization” scenarios peak to similar values to the ones we find ($[\ell(\ell+1)C_\ell/(2\pi)]_{\text{max}} \sim 10^{-12}$) again at $\ell \sim 2000$, but have a very different assumed reionization histories than any of our simulations. They found that the kSZ post-reionization contribution dominates the patchy signal at the scales of interest, while we find that the two signals are comparable in magnitude.

6. SUMMARY

We have derived the kSZ CMB anisotropies due to the inhomogeneous reionization of the universe. This is the first such calculation based on detailed, large-scale radiative transfer simulations of this epoch. As we have shown above, these simulations follow large enough volume to capture the full range of scales relevant to the large-scale reionization geometry. They also include most of the velocity fluctuations power, which is not the case for smaller-box simulations. We have also approximately corrected for the velocity power still missing from the box. The resulting sky power spectra peak at $\ell = 2000 - 8000$ with maximum values of $[\ell(\ell+1)C_\ell/(2\pi)]_{\text{max}} \sim 1 \times 10^{-12}$. The angular scale of the peak roughly corresponds to the typical ionized bubble sizes observed in our simulations, which is $\sim 5 - 20$ Mpc, depending on the assumed source efficiencies and the gas clumping at small scales. The kSZ anisotropy signal from reionization dominates the primary CMB signal above $\ell = 3000$. At large scales the patchy kSZ signal depends largely on the source efficiencies and the large-scale velocity fields. It is higher when sources are more efficient at producing ionizing photons, since such sources produce large ionized regions, on average, than less efficient sources. The introduction of sub-grid gas clumping in the radiative transfer simulations produce significantly more power at small scales, but has little effect at large scales. The sub-grid gas clumping also significantly enhances the non-Gaussianity of the kSZ maps, resulting in up to one order of magnitude more of the brightest kSZ regions than a Gaussian would predict. The integrated kSZ signal is strong enough to be detected by upcoming experiments, like ACT and SPT. However, the separation of the patchy reionization signal from the contribution by the fully-ionized gas after reionization seems difficult.

Our current simulations do not include the smallest atomically-cooling ionizing sources, these with total mass $10^8 M_\odot \lesssim M_{\text{tot}} < 2.5 \times 10^9 M_\odot$, as these are not resolved in our base N-body simulations. These smaller sources have important effects on the early global reionization history, but are also strongly suppressed due to Jeans-mass filtering in the ionized regions (Iliev et al. 2006c). During most of the evolution the reionization process is thus dominated by the larger sources, which are resolved here, and which dictate the large-scale reionization geometry. Consequently, we do not expect that the presence of the low-mass ionizing sources would change our current conclusions significantly.

This work was partially supported by NASA Astrophysical Theory Program grants NAG5-10825 and

NNG04G177G to PRS.

REFERENCES

- Box, G. E. P. & Muller, M. E. 1958, *Ann. Math. Stat.*, 29, 610
- Bunker, A., Stanway, E., Ellis, R., McMahon, R., Eyles, L., & Lacy, M. 2006, *New Astronomy Review*, 50, 94
- Ciardi, B. & Madau, P. 2003, *ApJ*, 596, 1
- Ciardi, B., Scannapieco, E., Stoehr, F., Ferrara, A., Iliev, I. T., & Shapiro, P. R. 2006, *MNRAS*, 366, 689
- Furlanetto, S., Oh, S. P., & Briggs, F. 2006, *ArXiv Astrophysics e-prints* (astro-ph/0608032)
- Furlanetto, S. R., Sokasian, A., & Hernquist, L. 2004a, *MNRAS*, 347, 187
- Furlanetto, S. R., Zaldarriaga, M., & Hernquist, L. 2004b, *ApJ*, 613, 1
- Gnedin, N. Y. & Jaffe, A. H. 2001, *ApJ*, 551, 3
- Gnedin, N. Y. & Prada, F. 2004, *ApJL*, 608, L77
- Gruzinov, A. & Hu, W. 1998, *ApJ*, 508, 435
- Haiman, Z. & Holder, G. P. 2003, *ApJ*, 595, 1
- Hu, W. 2000, *ApJ*, 529, 12
- Iliev, I. T., et al. 2006a, *MNRAS*, 371, 1057
- Iliev, I. T., Mellema, G., Pen, U.-L., Merz, H., Shapiro, P. R., & Alvarez, M. A. 2006b, *MNRAS*, 369, 1625
- Iliev, I. T., Mellema, G., Shapiro, P. R., & Pen, U. L. 2006c, *MNRAS*, submitted (astro-ph/0607517)
- Iliev, I. T., Pen, U.-L., Bond, J. R., Mellema, G., & Shapiro, P. R. 2006d, *New Astronomy Reviews*, in press (astro-ph/0607209)
- Iliev, I. T., Scannapieco, E., Martel, H., & Shapiro, P. R. 2003, *MNRAS*, 341, 81
- Iliev, I. T., Scannapieco, E., & Shapiro, P. R. 2005a, *ApJ*, 624, 491
- Iliev, I. T., Shapiro, P. R., Ferrara, A., & Martel, H. 2002, *ApJL*, 572, L123
- Iliev, I. T., Shapiro, P. R., & Raga, A. C. 2005b, *MNRAS*, 361, 405
- Jaffe, A. H. & Kamionkowski, M. 1998, *Phys. Rev. D*, 58, 043001
- Kaiser, N. 1984, *ApJ*, 282, 374
- Ma, C.-P. & Fry, J. N. 2002, *Physical Review Letters*, 88, 211301
- Malhotra, S. & Rhoads, J. 2006, *ApJ*, 647, 95L
- McQuinn, M., Furlanetto, S. R., Hernquist, L., Zahn, O., & Zaldarriaga, M. 2005, *ApJ*, 630, 643
- Mellema, G., Iliev, I. T., Alvarez, M. A., & Shapiro, P. R. 2006a, *New Astronomy*, 11, 374
- Mellema, G., Iliev, I. T., Pen, U. L., & Shapiro, P. R. 2006b, *MNRAS*, in press (astro-ph/0603518)
- Merz, H., Pen, U.-L., & Trac, H. 2005, *New Astronomy*, 10, 393
- Ostriker, J. P. & Vishniac, E. T. 1986, *ApJL*, 306, L51
- Rhoads, J. E., et al. 2003, *AJ*, 125, 1006
- Salvatterra, R., Ciardi, B., Ferrara, A., & Baccigalupi, C. 2005, *MNRAS*, 360, 1063
- Santos, M. G., Cooray, A., Haiman, Z., Knox, L., & Ma, C.-P. 2003, *ApJ*, 598, 756
- Scott, D. & Rees, M. J. 1990, *MNRAS*, 247, 510
- Seljak, U. & Zaldarriaga, M. 1996, *ApJ*, 469, 437
- Shapiro, P. R., Ahn, K., Alvarez, M. A., Iliev, I. T., Martel, H., & Ryu, D. 2006, *ApJ*, 646, 681
- Shapiro, P. R., Iliev, I. T., & Raga, A. C. 2004, *MNRAS*, 348, 753
- Spergel, D. N. et al. 2003, *ApJS*, 148, 175
- Springel, V., White, M., & Hernquist, L. 2001, *ApJ*, 549, 681
- Stanway, E. R. & et al. 2004, *ApJL*, 604, L13
- Sunyaev, R. A. & Zeldovich, I. B. 1980, *MNRAS*, 190, 413
- Tozzi, P., Madau, P., Meiksin, A., & Rees, M. J. 2000, *ApJ*, 528, 597
- Vishniac, E. T. 1987, *ApJ*, 322, 597
- Zahn, O., Zaldarriaga, M., Hernquist, L., & McQuinn, M. 2005, *ApJ*, 630, 657
- Zeldovich, Y. B. & Sunyaev, R. A. 1969, *Ap&SS*, 4, 301
- Zhang, P., Pen, U.-L., & Trac, H. 2004, *MNRAS*, 347, 1224